The Astrophysical Journal, 982:8 (15pp), 2025 March 20 https://doi.org/10.3847/1538-4357/adb3a5

Where is the Supervirial Gas? II. Insight from the Survey of Galactic Sightlines

Manami Roy[1,2], Smita Mathur[1,2], Sanskriti Das[3,6], Armando Lara-DI[4], Yair Krongold[4], and Anjali Gupta[5]
[1] Center for Cosmology and Astro Particle Physics (CCAPP), The Ohio State University, 191 W. Woodruff Avenue, Columbus, OH 43210, USA; roy.516@osu.edu
[2] Department of Astronomy, The Ohio State University, 140 W. 18th Avenue, Columbus, OH 43210, USA
[3] Kavli Institute for Particle Astrophysics and Cosmology, Stanford University, 452 Lomita Mall, Stanford, CA 94305, USA
[4] Instituto de Astronomia, Universidad Nacional Autonoma de Mexico, 04510 Mexico City, Mexico
[5] Columbus State Community College, 550 E Spring Street, Columbus, OH 43210, USA
Received 2024 November 22; revised 2025 January 19; accepted 2025 February 2; published 2025 March 11

Abstract

Recent observations have revealed a supervirial temperature gas phase at $\log(T/\mathrm{K}) \sim 7$ in the Milky Way, challenging existing galaxy formation models. This hot gas phase was discovered toward extragalactic absorption sightlines and blank-sky emission fields, both at high Galactic latitudes. The location of this hot component is unknown; is it in the extended circumgalactic medium (CGM) or in the interstellar medium (ISM) instead? We analyzed X-ray spectra from Chandra's High-Energy Transmission Grating observations of 27 Galactic X-ray binaries (XRBs) to investigate whether the hot gas component is present in the ISM. We searched for absorption lines of S XVI Kα, Si XIV Kα, and Ne X Kα, which are the telltale signatures of the hot gas and which have been detected toward extragalactic sightlines. Of the 27 targets, these lines were detected in the spectra of only 7, with two sources displaying broad line features likely intrinsic to the XRB systems. Additionally, most of the detected lines are time variable, reinforcing their likely association with the XRBs. Our results suggest that the supervirial temperature gas is not a widespread component of the ISM but may instead be located in extraplanar regions or the extended CGM, which aligns with some recent simulation results.

Unified Astronomy Thesaurus concepts: Circumgalactic medium (1879); Galaxy evolution (594); X-ray astronomy (1810)

1. Introduction

Galaxies, the fundamental building blocks of our Universe, have primary components such as a star-forming disk and the interstellar medium (ISM), a complex, multiphase environment within the disk containing a mix of dust, molecules, and atoms. Above and below the Galactic disk lies a more diffuse and ionized region compared to the ISM, known as the circumgalactic medium (CGM; for a review, see J. Tumlinson et al. 2017 and S. Mathur 2022).

Detections of Si II, Si III, Si IV, Ne IX, O VI, and O VII along with neutral atomic and molecular hydrogen from the Milky Way's ISM have revealed its diverse composition, encompassing various gas phases. These elements can be ionized and dispersed by energetic events such as stellar winds, supernova explosions, and interactions within binary star systems throughout their surroundings. Also, observations from the Cosmic Origins Spectrograph on the Hubble Space Telescope, as well as from XMM-Newton and Chandra, have revealed the multiphase nature of the CGM gas around Milky Way and Milky Way–like galaxies in both UV (e.g., K. Sembach et al. 2003; J. Tumlinson et al. 2011; J. K. Werk et al. 2016; P. Richter et al. 2017) and X-ray (e.g., F. Nicastro et al. 2002; R. J. Williams et al. 2005; D. B. Henley et al. 2010; A. Gupta et al. 2012; T. Fang et al. 2015; S. Das et al. 2021). In contrast to the Galactic disk, where energetic processes account for the observed ionized elements in the ISM, the CGM does not have a well-defined mechanism for producing and ionizing gas. Numerical simulations suggest that feedback processes from star formation activities and active galactic nuclei, which expel ionized metals from the disk and the nucleus into the CGM, play a significant role in shaping the CGM.

Based on these observations, the CGM was thought to have three phases: virial warm–hot gas ($\log(T/\mathrm{K}) \sim 6$–6.5), warm gas ($\log(T/\mathrm{K}) \sim 5$–5.5), and cool gas ($\log(T/\mathrm{K}) < 4$). However, this understanding was shaken with the recent discovery of the supervirial component ($\log(T/\mathrm{K}) \sim 7$–7.5 (S. Das et al. 2019b) in the Milky Way CGM using absorption lines from XMM-Newton observations toward the blazar IES 1553+113. Since then, multiple detections of this hotter supervirial gas have been made in both emission and absorption (e.g., S. Das et al. 2019a; J. Bluem et al. 2022; J. Bhattacharyya et al. 2023; A. Gupta et al. 2023; A. Lara-DI et al. 2023; R. L. McClain et al. 2024). For example, S. Das et al. (2019a) detected the supervirial component in emission along the same sightline of IES 1553 +113 using XMM-Newton. A. Gupta et al. (2021) identified this component and the virial component across four sightlines in emission using Suzaku data. Later, J. Bhattacharyya et al. (2023) also observed this supervirial gas in the Milky Way's CGM in emission toward the blazar Mrk 421 and five other nearby sightlines. In a recent study, R. L. McClain et al. (2024) detected the Ne X line, associated with supervirial temperature gas, along the sightline to NGC 3783, and A. Lara-DI et al. (2023) used stacked X-ray spectral observations toward multiple extragalactic sightlines to detect Si XIV Kα and S XVI Kα lines, the signature of the supervirial temperature gas in the Milky Way's CGM. Additionally, it was found that the supervirial temperature hot component is not limited to specific sightlines and is detected all across the sky by all-sky surveys in both absorption (A. Lara-DI et al. 2023, 2024) and emission (J. Bluem et al. 2022; A. Gupta et al. 2023; G. Ponti et al. 2023).

[6] Hubble Fellow.

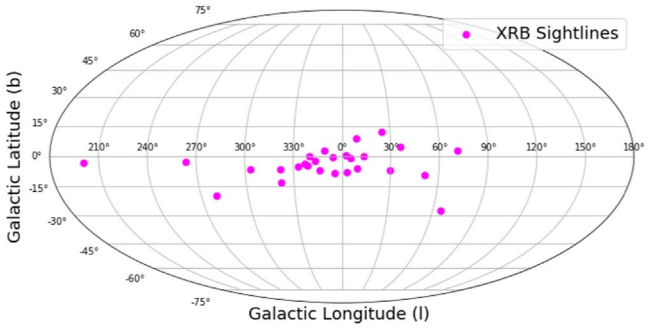

Figure 1. Skyplot of the sample of 27 XRBs we analyze in this work, showing their Galactic latitude and longitude.

For the Milky Way mass galaxy, the virial component of the CGM gas is predicted by galaxy formation simulations, but the gas at $\log(T/\mathrm{K}) \sim 7$–$7.5$ was not predicted. It raises several important questions about the origin and location of the supervirial gas. Is it truly from the CGM, or is it in the ISM or the extraplanar region outside the ISM? To answer these questions, we examine Chandra's High-Energy Transmission Grating (HETG) X-ray observations of Galactic X-ray binaries (XRBs). In the pilot study, A. Lara-DI et al. (2024) analyzed three XRB sightlines and did not detect the supervirial hot gas. However, to conclude that this phase is not present in the ISM, it is important to study a large sample with all-sky coverage and better statistics. Therefore, we survey a large extended sample of 27 XRBs and look for the Ne X, Si XIV, and S XVI absorption lines, which are the telltale signs of the supervirial hot component and which have been previously detected along extragalactic sightlines. This experiment is similar to that done by F. Nicastro et al. (2016b) to separate the ISM and CGM components of the virial temperature gas traced by the O VII absorption line ($\lambda = 21.602$ Å). These authors found that the O VII-bearing gas permeates both the ISM and the CGM, but the column density in extragalactic sightlines is dominated by the CGM.

This paper is organized as follows: Section 2 details the data sample, while Section 3 outlines the data analysis methodology. In Section 4, we present our findings, followed by a discussion of their implications in Section 5. Finally, our conclusions are summarized in Section 6.

2. Data

We obtained archival Chandra ACIS-S HETG observations for 27 XRBs, which were taken from the sample used by F. Nicastro et al. (2016a) and E. Gatuzz et al. (2021). We show the location of our XRB sample in terms of Galactic latitude and longitude in Figure 1. This data set includes approximately 190 observations, with a total combined exposure time of 5758 ks (see Table 1).

The observations were reprocessed using the "*chandra_repro*" script within the Chandra Interactive Analysis of Observations (CIAO) software, version 4.13. We then combined the spectra using the "combine_grating_spectra" command in CIAO, resulting in four stacked spectra for each XRB: one for the High Energy Gratings (HEG) continuous clocking (CC) mode observations, another for the HEG timed exposure (TE) mode observations, a third for the Medium Energy Gratings (MEG) CC observations, and a final one for the MEG TE observations. Thus we created 27×4 spectra, which were analyzed as discussed in Section 3. The MEG has a resolving power ($\lambda/\Delta\lambda$) of 1000 at 12.4 Å, while the HEG has an $\lambda/\Delta\lambda$ of 660 at 15 Å.

In the 4–19 Å spectral range, TE observations can be significantly affected by pileup when the sources are in a high-flux state (e.g., D. Rogantini et al. 2021). Pileup occurs when multiple photons are recorded as a single event, resulting in information loss and spectral distortion. However, pileup minimally impacts narrow absorption features from grating spectra, as described by D. Rogantini et al. (2021). Grating spectra mitigate the effects of pileup due to the fundamental mechanism of photon dispersion. Moreover, as the narrow absorption lines are confined to specific energy ranges, they correspond to distinct spatial locations on the detector in grating mode. Therefore, the likelihood of multiple photons arriving simultaneously at those specific energies corresponding to these narrow features is low. Additionally, the continuum distortion caused by pileup, where low-energy photons are shifted to higher energies, is minimized in grating mode. The dispersion spreads the continuum flux over a larger area, making the effects of pileup less concentrated. As a result, the contrast between the absorption line and the continuum remains largely intact, enhancing the detectability of weak or narrow lines. Therefore, we analyzed both TE and CC spectra for all these targets, focusing on the narrow absorption features.

3. Analysis

For our spectral fitting, we employed the XSPEC software (v12.13.0) and used chi-squared (χ^2) statistics to analyze the CC MEG and HEG spectra of our sample XRBs with a high signal-to-noise ratio of > 50. We conducted a similar analysis for the TE observations.

Following A. Lara-DI et al. (2024), our spectral modeling focused on the region within ± 0.25 Å around the rest wavelengths of the ionic transitions of interest: S XVI Kα ($\lambda = 4.729$ Å), Si XIV Kα ($\lambda = 6.182$ Å), and Ne X Kα ($\lambda = 12.134$ Å).

Initially, we fitted the local continuum within these narrow spectral ranges using a power-law model (XSPEC model *pow*). The power-law models for the different spectral regions were allowed to vary independently. If additional spectral features were present, we included a Gaussian profile (XSPEC model *agauss*) to account for them.

Next, we modeled the potential presence of absorption features with a narrow Gaussian profile centered at the rest wavelengths of S XVI Kα, Si XIV Kα, and Ne X Kα. The position of each Gaussian profile was set to the expected line value, with an allowed variation of ± 0.012 Å in some cases to account for the resolution element of HEG and ± 0.023 Å for the resolution element of MEG. We fixed the line width to 0 Å (as the lines are unresolved at HETG resolution) and allowed the normalization to vary. In some cases, we also fit with a broad Gaussian line (with nonzero line width) or two narrow Gaussian lines, as required by the data (see Section 4).

4. Results

For the 27 XRBs, we have $27 \times 4 = 108$ spectra (HEG +MEG+CC+TE) and $108 \times 3 = 324$ possible detections for the three lines (S XVI Kα, Si XIV Kα, and Ne X Kα). We detected only 25 lines with 3σ or better significance: 2 of Ne X, 14 of Si XIV, and 9 of S XVI. All the detected lines were in the

Table 1
Galactic Source Description

Source	Galactic Latitude (degree)	Distance (kpc)	Height (kpc)	Obs. ID	Exp. Time (ks)	Exp. Mode
4U 1636-53	−4.818	6.0	0.5	6635	23.07	CC
				105	29.40	CC
				1939	26.29	TE
				22701	46.61	TE
				22936	30.13	TE
				24625	29.09	TE
				24626	24.40	TE
				20791	62.93	TE
				21099	31.99	TE
				21100	32.95	TE
EXO 0748-676	−19.811	8.0; 5.7	2.88, 2.05	1017	47.99	TE
				4573	162.89	TE
				4574	123.54	TE
PSRB 0833-45	−2.787	0.3	0.015	131	35.95	CC
SAX J1808.4-3658	−8.148	2.8	0.4	6297	14.29	CC
Swift J1753.5-0127	+12.186	⋯	⋯	14428	20.02	CC
Swift J1910.2-0546	−6.844	⋯	⋯	14634	29.96	CC
4U 1728-16 (GX 9+9)	+9.038	4.4; 7.5	0.69, 1.19	703	20.72	TE
				11072	95.84	TE
V*V821Ara (GX 339-4)	−4.326	10.0	0.76	4569	49.90	CC
				4570	38.90	CC
				4571	35.32	CC
				4420	74.05	TE
				5475	37.39	TE
				6290	21.22	TE
GS 1826-238	−6.088	7.5	0.8	2739	68.23	TE
4U 2129+12	−27.312	5.8	2.99	675	19.80	TE
				4572	59.17	TE
				27459	9.33	TE
4U 1543-624	−6.337	7.0	0.77	702	27.40	TE
XTE J1650-500	−3.427	⋯	⋯	2699	19.21	CC
				2700	28.50	CC
				3400	10.00	TE
				3401	9.51	TE
4U 1254-69	−6.4	13.0 ± 3.0	1.45 ± 0.3	3823	51.69	TE
4U 1957+11	−9.33	⋯	⋯	10660	18.98	CC
				4552	65.60	TE
				10659	9.87	TE
				10661	9.82	TE
4U 0614+091	−3.36	2.2 ± 0.7	0.13 ± 0.04	10759	58.88	TE
				10760	44.10	TE
				10857	57.28	TE
				10858	34.36	TE
4U 1705-44	−2.34	7.6 ± 0.3	0.3 ± 0.01	1924	5.86	CC
				1923	24.41	TE
				5500	26.47	TE
				18086	23.95	TE
				19451	37.98	TE
				20082	69.40	TE
4U 1728-34	−0.15	5.2 ± 0.5	0.014 ± 0.001	6567	151.25	CC
				6568	49.30	CC
				7371	39.56	CC
				2748	29.62	TE

Table 1
(Continued)

Source	Galactic Latitude (degree)	Distance (kpc)	Height (kpc)	Obs. ID	Exp. Time (ks)	Exp. Mode
				19452	20.23	TE
				20106	58.42	TE
				20107	32.43	TE
4U 1735-44	−6.99	9.4 ± 1.4	1.15 ± 0.17	6637	24.09	CC
				6638	23.03	CC
				704	24.35	TE
				25248	26.18	TE
				25897	14.41	TE
				25898	10.71	TE
				25899	33.82	TE
				25900	14.41	TE
				25901	24.06	TE
				27532	17.00	TE
				27917	24.25	TE
				28919	22.32	TE
4U 1820-30	−7.91	7.6 ± 0.4	1.05 ± 0.05	6633	25.08	CC
				6634	25.03	CC
				22276	13.65	CC
				22277	14.62	CC
				24698	25.54	CC
				25029	25.86	CC
				25030	23.49	CC
				25031	22.99	CC
				25032	20.04	CC
				25033	23.38	CC
				25037	17.81	CC
				25038	15.50	CC
				7032	46.16	CC
				1021	9.64	TE
				1022	10.65	TE
4U 1626-67	−13.09	$3.5^{+0.2}_{-0.3}$	$0.8^{+0.1}_{-0.1}$	104	39.48	TE
				3504	94.81	TE
				11058	76.87	TE
				17448	48.90	TE
				21686	45.88	TE
				24700	11.76	TE
				24768	17.13	TE
				26204	17.13	TE
				26250	12.73	TE
				26009	56.81	TE
				26086	29.34	TE
				27954	29.34	TE
				27960	16.16	TE
				28366	14.50	TE
				19782	19.85	TE
				20909	25.14	TE
Serpens X-1	4.84	11.1 ± 1.6	0.94 ± 0.13	16208	142.04	CC
				16209	156.54	CC
				700	76.42	TE
				17485	83.26	TE
				17600	37.05	TE
Cygnus X-1	−11.31	13.4 ± 2.0	2.7 ± 0.4	1511	12.62	CC
				2415	30.02	CC
				3407	16.07	CC
				3724	8.10	CC
				3815	55.63	CC
				12314	0.90	CC
				12472	3.31	CC
				107	11.40	TE
				2741	1.89	TE

Table 1
(Continued)

Source	Galactic Latitude (degree)	Distance (kpc)	Height (kpc)	Obs. ID	Exp. Time (ks)	Exp. Mode
				2742	1.87	TE
				2743	2.42	TE
				3814	47.19	TE
				8525	29.43	TE
				9847	18.86	TE
				11044	29.43	TE
				12313	2.14	TE
				13219	4.42	TE
				16735	17.57	TE
				26685	7.19	TE
				29064	9.06	TE
GX 349+2	2.74	9.2	0.44	6628	12.54	CC
				7336	12.06	CC
				12199	18.77	CC
				13221	16.52	CC
				13222	25.81	CC
				715	9.42	TE
				14256	9.30	TE
				3354	17.45	TE
				13220	18.87	TE
				18084	20.42	TE
GX 340+00	−0.07	11.0 ± 0.3	0.0130 ± 0.0004	1922	5.82	CC
				6631	25.03	CC
				6632	23.57	CC
				1921	23.36	TE
				18085	24.11	TE
				19450	60.15	TE
				20099	60.62	TE
GX 5-1	−1.02	9.2	0.16	10691	8.05	CC
				10692	8.15	CC
				10693	8.11	CC
				10694	3.75	CC
				5888	44.98	CC
				716	8.91	TE
				22411	15.67	TE
				22412	17.56	TE
				22413	16.25	TE
				22414	17.28	TE
				22415	15.76	TE
				22416	14.00	TE
				19449	80.49	TE
				20119	12.10	TE
GX 3+1	0.79	$5.0^{+0.8}_{-0.7}$	$0.07^{+0.01}_{-0.009}$	2745	8.96	CC
				24701	20.38	TE
				24769	27.15	TE
				24770	17.48	TE
				26432	21.06	TE
				26434	11.68	TE
				27271	10.25	TE
				27272	9.79	TE
				27273	9.79	TE
				16307	43.59	TE
				16492	43.59	TE
				18615	12.16	TE
				19890	29.08	TE
				19907	26.01	TE
				19957	29.08	TE
				19958	29.08	TE
GX 13+1	0.10	7 ± 1	0.01 ± 0.002	11818	24.41	CC

Table 1
(Continued)

Source	Galactic Latitude (degree)	Distance (kpc)	Height (kpc)	Obs. ID	Exp. Time (ks)	Exp. Mode
				13197	10.09	CC
				2708	29.35	TE
				11814	28.12	TE
				11815	28.12	TE
				11816	28.12	TE
				11817	28.12	TE
				20191	24.25	TE
				20192	22.32	TE
				20193	24.25	TE
				20194	24.56	TE

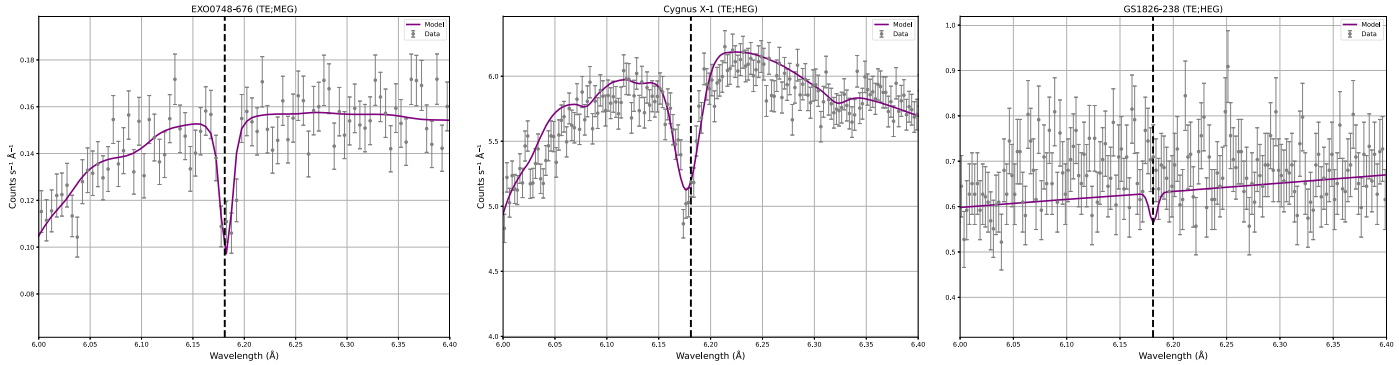

Figure 2. Examples of Si XIV Kα line profiles observed in three XRB sources. The black points with error bars represent the data, which are fit using power-law and Gaussian models (shown in solid purple lines): a narrow Gaussian (left panel), a broad Gaussian (middle panel), and a 3σ upper limit (right panel). Summary: the narrow and broad Gaussian fits capture the 3σ detected Si XIV line, while the 3σ upper limit represents cases with no significant line detection. The vertical dashed lines indicate the expected rest wavelength of the Si XIV transition.

spectra of 7 XRBs (out of 27), as shown in Figure 2 and Table 2.

Of the 25 detected lines, 16 appeared to be resolved. Therefore, we fit them with broad Gaussian profiles or with two narrow Gaussian (marked by double stars in the table where we quoted the values for the fit with a broad Gaussian). All the results are summarized in Table 2, where the columns (left to right) are the names of the sources, exposure mode, grating name, and line equivalent width (EW). The errors quoted are 1σ, and the bold numbers are the lines where we got at least 3σ detections. The values without error bars are 1σ upper limits. In Figure 2, we show examples of Si XIV line profiles toward three XRB sightlines (with a narrow Gaussian in the left panel, a broad Gaussian in the middle panel, and a 3σ upper limit in the right panel). The narrow and broad Gaussian fits show the 3σ detections of the Si XIV line, while the 3σ upper limit represents cases with no significant line detection. The vertical dashed lines indicate the expected rest wavelength of the Si XIV transition.

4.1. Detection or Not?

Among all the detections, for four of the sources, we noticed that there are detections of Si XIV in MEG but not in HEG. HEG has a lower effective area in the relevant energy range than MEG, but the upper limits of HEG are lower than MEG detections. Therefore, we investigate these cases further. We simultaneously fit the spectra from HEG and MEG and look for the Si XIV line. We summarize our finding in Table 3, where the third column denotes the EW of the individual fitting, and the fourth column denotes the EW of the simultaneous fitting of HEG and MEG spectra. As anticipated, the EWs of all of these four detections have decreased, and now the line is detected in both HEG and MEG. However, the detection significance has decreased from more than 3σ to close to 3σ.

5. Discussion

Different studies have identified a warm–hot gas phase in the Milky Way's ISM with a temperature around $\log(T/\mathrm{K}) \sim 6$ (e.g., F. Nicastro et al. 2016a). Ne IX originates from this gas phase and has been detected in the sightlines analyzed in these studies. In contrast, ions like Ne X, Si XIV, and S XVI, which indicate even hotter gas, have not been observed in the spectra of most of these XRBs. Additionally, there are no known detections of these higher charge states in the Galactic ISM in existing literature. This implies that while gas at $\log(T/\mathrm{K}) \sim 6$ is commonly present in the ISM, the hotter gas is rare. Therefore, the contribution of the ISM to the supervirial hot component observed in extragalactic sightlines is minimal at best and much lower than the contribution from the warm–hot component (e.g., F. Nicastro et al. 2016a).

Additionally, we compare the line detection limits for the Galactic XRB sightlines to those for the extragalactic lines of sight. For EXO 0748-676, the EW limits for Si XIV are higher,

Table 2
Best-fit Parameter Value

Source	Exp. Mode	Grating	EW (mA)[a]		
			Ne X (12.132 A)	Si XIV (6.181 A)	S XVI (4.728 A)
4U 1636-53	CC	HEG	-2.11	-0.63	-0.32
		MEG	-1.26	-0.28	-0.19
	TE	HEG	-1.92	-0.06	-0.4
		MEG	-0.44	$\mathbf{-1.04}^{+0.2}_{-0.2}$	$-0.33^{+0.28}_{-0.28}$
EXO 0748-676	TE	HEG	$-5.17^{+4.14}_{-4.14}$	$\mathbf{-5.11}^{+0.7}_{-0.7}$	$\mathbf{-3.19}^{+0.95}_{-0.95}$
		MEG	-4.34	$\mathbf{-6.43}^{+0.68}_{-0.68}$	$-1.52^{+1.0}_{-1.0}$
PSR B0833-45	CC	HEG	-4.55	$-4.28^{+2.68}_{-2.68}$	-3.89
		MEG	-5.15	-4.46	-7.75
SAX J1808.4-3658	CC	HEG	$-2.21^{+2.21}_{-2.21}$	-0.35	-3.01
		MEG	-1.7	-0.2	-2.59
Swift J1753.5-0127	CC	HEG	-0.46	$0.83^{+0.63}_{-0.63}$	$-1.99^{+1.16}_{-1.16}$
		MEG	-0.97	-0.15	-1.92
Swift J1910.2-0546	CC	HEG	-0.66	-0.11	-0.29
		MEG	$-0.52^{+0.41}_{-0.41}$	$-0.43^{+0.24}_{-0.24}$	-0.62
4U 1728-16 (GX9+9)	TE	HEG	-0.74	-0.17	$-0.26^{+0.23}_{-0.23}$
		MEG	$-0.51^{+0.46}_{-0.46}$	$\mathbf{-0.73}^{+0.18}_{-0.18}$	-0.42
V*V821Ara (GX 339-4)	CC	HEG	$-0.56^{+0.31}_{-0.31}$	-0.02	-0.17
		MEG	-0.2	-0.01	-0.03
	TE	HEG	-1.46	-0.27	-0.14
		MEG	-0.34	$\mathbf{-0.84}^{+0.23}_{-0.23}$	-0.22
GS1826-238	TE	HEG	-7.94	-0.5	-0.83
		MEG	-1.54	$-0.59^{+0.55}_{-0.55}$	-1.34
4U 2129+12	TE	HEG	-2.09	-0.24	-0.63
		MEG	-0.65	-0.15	-0.70
4U 1543-624	TE	HEG	-3.43	-1.73	-2.02
		MEG	-0.96	-0.33	-0.5
XTE J1650-500	CC	HEG	-0.03 (c)	$-0.16^{+0.15}_{-0.15}$	-0.06
		MEG	0.22	$-0.13^{+0.12}_{-0.12}$	-0.17
XTE J1650-500	TE	HEG	NE	NE	NE
		MEG	NE	NE	NE
4U 1254-69	TE	HEG	-3.85	-1.23	$-2.17^{+1.11}_{-1.11}$
		MEG	-1.63	$-1.1^{+0.58}_{-0.58}$	-0.77
4U 1957+11	CC	HEG	-6.29	-0.6	-0.79
		MEG	-2.08	$-0.96^{+0.81}_{-0.81}$	-0.54
	TE	HEG	-1.13	-0.74	$-0.76^{+0.51}_{-0.51}$
		MEG	-0.26	-0.69	-0.66
4U 0614+091	TE	HEG	-0.43	-0.36	-0.51
		MEG	-0.13	$-0.58^{+0.23}_{-0.23}$	-0.16
4U 1705-44	CC	HEG	-35.05	-0.62	-0.36
		MEG	$-13.44^{+10.24}_{-11.54}$	-0.21	-0.40
	TE	HEG	-18.6	-0.11	-0.1
		MEG	-2.17	-0.1	$-0.39^{+0.28}_{-0.28}$
4U 1728-34	CC	HEG	-3.8	-0.37	-0.31
		MEG	-1.96	$-0.25^{+0.21}_{-0.21}$	$-0.66^{+0.23}_{-0.23}$
	TE	HEG	-736.24	-0.74	-0.36
		MEG	-131.7	-0.43	-0.69
4U 1735-44	CC	HEG	-2.05	-0.07	$-0.48^{+0.43}_{-0.43}$
		MEG	$-0.89^{+0.81}_{-0.81}$	-0.31	-0.68

Table 2
(Continued)

Source	Exp. Mode	Grating	EW (mA)[a]		
			Ne X (12.132 A)	Si XIV (6.181 A)	S XVI (4.728 A)
	TE	HEG	-2.11	-0.31	-0.13
		MEG	$-1.06^{+1.05}_{-1.05}$	$-0.59^{+0.44}_{-0.44}$	$-0.87^{+0.61}_{-0.61}$
4U 1820-30	CC	HEG	$1.09^{+0.41}_{-0.41}$	-0.05	-0.36
		MEG	-0.07	-0.14	-0.4
	TE	HEG	$-1.41^{+1.11}_{-1.11}$	-0.42	-0.57
		MEG	-0.33	$\mathbf{-1.61}^{+0.42}_{-0.42}$	-0.39
4U 1626-67	TE	HEG	-0.21 (-2.01)	-0.46	-0.65
		MEG	-0.06 ($-0.91^{+0.87}_{-0.87}$)	-0.34	-0.22
Serpens X-1	CC	HEG	-1.13	-0.02	-0.03
		MEG	-0.28	-0.01	-0.07
	TE	HEG	1.18	-0.05	-0.07
		MEG	-0.29	$-0.18^{+0.16}_{-0.16}$	-0.06
Cygnus X-1	CC	HEG	$\mathbf{-2.52}^{+0.2}_{-0.19}$ [b]	$\mathbf{-4.59}^{+0.15}_{-0.13}$[b]	$\mathbf{-2.69}^{+0.24}_{-0.23}$[b]
		MEG	$\mathbf{-1.74}^{+0.36}_{-0.22}$[b]	$\mathbf{-6.07}^{+0.12}_{-0.12}$[b]	$\mathbf{-2.85}^{+0.34}_{-0.21}$[b]
	TE	HEG	-0.31	$\mathbf{-5.47}^{+0.19}_{-0.46}$[b]	$\mathbf{-3.19}^{+0.34}_{-0.34}$[b]
		MEG	-1.07	$\mathbf{-4.63}^{+0.25}_{-0.25}$[b]	$\mathbf{-2.21}^{+0.25}_{-0.29}$[b]
GX 349+2	CC	HEG	-1.27	-0.14	-0.18
		MEG	-0.79	-0.13	-0.11
	TE	HEG	-1.2	-0.17	$-0.22^{+0.2}_{-0.2}$
		MEG	-0.98	-0.6	-0.15
GX 340+00	CC	HEG	-18.74	-0.89	-0.49
		MEG	-11.27	-0.32	-0.12
	TE	HEG	-1806	-0.26	-0.32
		MEG	-640	-0.09	-0.21
GX 5-1	CC	HEG	-13.75	-0.12	$-0.42^{+0.2}_{-0.2}$
		MEG	-11.22	-0.23	-0.37
	TE	HEG	-358.16	-0.19	-0.10
		MEG	-89.94	-0.15	$-0.25^{+0.13}_{-0.13}$
GX 3+1	CC	HEG	-24.2	-0.19	-0.57
		MEG	$-12.97^{+8.38}_{-9.33}$	-1.15	-0.33
	TE	HEG	-1134.6	-0.13	-0.17
		MEG	-3.91	-0.25	-0.11
GX 13+1	CC	HEG	-19.15	$\mathbf{-6.38}^{+0.75}_{-0.75}$[b]	$\mathbf{-2.8}^{+0.5}_{-0.38}$
		MEG	-19.14	$\mathbf{-5.47}^{+0.58}_{-0.44}$[b]	$\mathbf{-2.99}^{+0.41}_{-0.41}$
	TE	HEG	-2968.09	$\mathbf{-7.15}^{+0.3}_{-0.27}$ [b]	$\mathbf{-4.75}^{+0.27}_{-0.26}$[b]
		MEG	$-11.98^{+10.47}_{-8.52}$	$\mathbf{-7.01}^{+0.17}_{-0.21}$[b]	$\mathbf{-4.52}^{+0.28}_{-0.12}$[b]

Notes.
[a] The 1σ errors are given; otherwise 1σ upper limits are quoted. Numbers are made bold whenever lines are detected with 3σ.
[b] Fitted with a broad Gaussian.

and for S XVI they are comparable with the extragalactic sightlines (comparing the EW from Table 2 in A. Lara-DI et al. 2023). For other XRB sightlines, narrow-line EW limits are ∼30–50 times lower than extragalactic sightlines. Typically, the detection limits for Galactic XRB sightlines are lower (i.e., weaker lines can be detected) because XRBs are bright X-ray sources. Extragalactic sources, on the other hand, are fainter, requiring much longer observation times to detect comparably weak lines.

Next, let us discuss the line detections and analyze whether they arise in the ISM or are intrinsic to the XRB source. We have tried to answer this question in three ways, as discussed below.

5.1. ISM or Intrinsic to XRB? From Variability Test

We performed a variability test whenever we had a detection. We take individual observations made at different times and fit the same line, which is detected in the stacked spectrum. We find that some of the detected lines are variable with time, whereas some of them are not. We note the EW of individual observations in the Table 4. We also plotted the EW

Table 3
Values of EW of Si XIV Detections after Simultaneous Fitting of Spectra from HEG and MEG

Source	Grating	EW_{sim} (mÅ)
4U 1636 [TE]	HEG	$-0.37^{+0.13}_{-0.14}$
	MEG	$-0.42^{+0.16}_{-0.15}$
4U 1728-16 (GX 9+9) [TE]	HEG	$-0.34^{+0.11}_{-0.11}$
	MEG	$-0.41^{+0.14}_{-0.14}$
V*V821Ara (GX 339-4) [TE]	HEG	$-0.42^{+0.15}_{-0.14}$
	MEG	$-0.48^{+0.16}_{-0.17}$
4U 1820-30 [TE]	HEG	$-0.76^{+0.26}_{-0.26}$
	MEG	$-0.99^{+0.34}_{-0.34}$

with time of observations for the detected lines in Figure 3 and summarized our finding in Table 4. In the left panel of Figure 3, we show five XRBs for which we can fit narrow lines, and in the right panel we show the individual ions of two XRBs fitted with broad lines. We discuss all the cases here.

1. In the case S XVI line in EXO 0748-676, the upper limit in 2001 is consistent with the 2003 detection and error bar. However, the two data points from 2003 do not coincide completely, which can be suggestive of variability. For the Si XVI line, the upper limit in 2001 is not consistent with the 2003 detections, suggesting variability.
2. For 4U 1820-30, the upper limit of Si XIV in 2001 is not consistent with the detection in the same year, indicating variability.
3. For Si XIV in the 4U 1728-16 spectra, we see a clear variability from the year 2000 to 2010.
4. For VstarV821Ara, the upper limit of S IXIV in 2003 is not consistent with the detection in 2005, suggesting variability.
5. For CygX1, the upper limits and detections vary with time for all the ions.
6. For GX 13+1, the upper limits and detections vary with time for all Si XIV and S XVI ions.

If the lines are variable, then they likely arise intrinsically in the XRB, and if they are not variable, then they might be intrinsic or might arise from the intervening medium. Therefore, as shown in Figure 3, most of the detected lines are variable and are most likely intrinsic to XRBs.

5.2. ISM or Intrinsic to XRB? From Line Width

The line width can also indicate whether lines are from the ISM or if they are intrinsic to the XRB source. For example, wind and large turbulence in the XRB may give rise to a broad profile. Alternatively, turbulence in the ISM can also broaden the line. Two narrow lines at slightly different heliocentric velocities may overlap and may also mimic a broad line.

For most of the detections, except for GX 13+1 and CygX1, the lines were well fitted with one narrow Gaussian line. However, for GX 13+1 and CygX1, the lines are broad, and we fit them with a broad Gaussian or two narrow Gaussians. However, we cannot choose between these two models based on the chi-squared value alone as the reduced chi-square is similar for both the fits. However, S. Das (2024) demonstrates that fitting two unresolved Gaussians with a single unresolved Gaussian does not significantly overestimate or underestimate the input EW, regardless of the line-of-sight velocities and amplitudes, ruling out the possibility that our data represent purely thermally broadened multiple components appearing as a single nonthermally broadened component.

Further, we measure the nonthermal broadening of these lines and find that in the case of CygX1 and GX 13+1, the broad lines (Si XIV and S XVI) have an FWHM of ∼1000 and ∼1200 km s^{-1}, respectively. The thermal FWHM of Si XIV and S XVI lines is 180 and 164 km s^{-1}, respectively, and the instrumental width is about ∼500–700 km s^{-1}. Thus the thermal width is not high enough to be resolved by HETG; however, the nonthermal width is well resolved and well above the instrumental width. Also, the nonthermal width is 2–5 times more than the thermal width, where broadening can rise from turbulence, wind from XRB, or turbulence in ISM.

However, note that the presence of the binary-related absorption lines can affect the detection of the weak ISM lines. In order to assess this, we calculate the upper limit of the detection of a narrow line by fitting the observed line with a broad line and one narrow line. We find that the EW limit of the narrow line is ∼30–50 times smaller than the EW of the broad line. This implies that the narrow line can be detected in the presence of a broad line even if the EW of the narrow line is 30–50 times smaller than the broad line EW.

5.3. ISM or Intrinsic to XRB? From Correlation with Galactic Distance and Height

Another way to check whether the lines are arising in the intervening medium is to investigate the correlation between the EW of the detected lines and the height from the Galactic plane, the distance from us, and the Galactic latitude. If the lines arise in the diffuse ISM, then the EW will increase with increasing distance and decreasing height and Galactic latitude, as we probe more of the disk and hence more of the ISM. We plotted the EWs with errors for the detected lines in Figure 4. We do not find any clear correlation with distance or height. Two Si XIV detections with large EWs are at high latitudes and high heights. However, one high EW detection is for a small height and small latitude. Thus this exercise indicates that most of the detected lines may not come from the diffuse ISM.

5.4. Comparison with Simulations

The origin and location of this newly discovered supervirial phase were also investigated by different hydrodynamical simulations. A. Vijayan & M. Li (2022) showed that stellar feedback can produce this phase. However, their required star formation rate was high compared to that of the Milky Way. M. S. Bisht et al. (2024) also claim that the supervirial hot phase arises from the heating of the virial hot gas by stellar feedback. Alternatively, M. Roy et al. (2024) showed the origin to be adiabatic compressive heating of the infalling virial hot gas. While the origin of the supervirial hot gas phase in different simulations is different, they all point out that this phase is in the extraplanar region of the Galaxy, which is in alignment with what we find in this paper. Observationally, we

Table 4
Variability Test

Source	Exp. Mode	Grating	Ion	Obs Id (Year of Obs)	EW[a] (mA)	Variable
4U 1636-53	TE	MEG	Si XIV	Total (XX)	$-1.04^{+0.2}_{-0.2}$	Yes
				105 (1999)	$-1.77^{+0.4}_{-0.4}$	
				1939 (2001)	$-1.01^{+0.37}_{-0.37}$	
				20791 (2018)	$-0.86^{+0.54}_{-0.54}$	
				21099 (2018)	−1.41	
				21100 (2018)	−0.91	
				22701 (2021)	−0.73	
				22936 (2021)	$-1.09^{+0.97}_{-0.97}$	
				24625 (2021)	−1.89	
				24626 (2021)	−2.1	
4U 1728-16 (GX 9+9)	TE	MEG	Si XIV	Total (XX)	$-0.73^{+0.18}_{-0.18}$	Yes
				703 (2000)	$-1.43^{+0.4}_{-0.4}$	
				11072 (2010)	$-0.56^{+0.2}_{-0.2}$	
VstarV821Ara (GX 339-4)	TE	MEG	Si XIV	Total (XX)	$-0.84^{+0.23}_{-0.23}$	Yes
				4420 (2003)	$-0.32^{+0.23}_{-0.23}$	
				5475 (2005)	$-3.92^{+2.55}_{-2.55}$	
				6290 (2005)	−20.6	
EXO 0748-676	TE	HEG	Si XIV	Total (XX)	$-5.11^{+0.7}_{-0.7}$	Yes
				1017 (2001)	−4.56	
				4573 (2003)	$-5.53^{+0.97}_{-0.97}$	
				4574 (2003)	$-5.19^{+1.3}_{-1.3}$	
			S XVI	Total (XX)	$-3.19^{+0.95}_{-0.95}$	No
				1017 (2001)	−7.99	
				4573 (2003)	$-3.14^{+1.46}_{-1.46}$	
				4574 (2003)	$-2.2^{+1.81}_{-1.81}$	
		MEG	Si XIV	Total (XX)	$-6.43^{+0.68}_{-0.68}$	Yes
				1017 (2001)	−6.16	
				4573 (2003)	$-7.28^{+0.9}_{-0.9}$	
				4574 (2003)	$-5.73^{+1.19}_{-1.19}$	
4U 1820-30	TE	MEG	Si XIV	Total (XX)	$-1.61^{+0.42}_{-0.42}$	Yes
				1021 (2001)	−1.12	
				1022 (2001)	$-2.58^{+0.57}_{-0.57}$	
GX 13+1	CC	HEG	Si XIV	Total (XX)	$-6.38^{+0.75}_{-0.75}$	Yes
				11818 (2010)	$-4.52^{+0.55}_{-1.01}$	
				13197 (2011)	$-9.41^{+1.34}_{-1.48}$	
		MEG	Si XIV	Total (XX)	$-5.47^{+0.58}_{-0.44}$	
				11818 (2010)	$-4.45^{+0.55}_{-0.73}$	
				13197 (2011)	$-7.52^{+0.65}_{-1.03}$	
	TE	HEG	Si XIV	Total (XX)	$-7.15^{+0.3}_{-0.27}$	
				2708 (2002)	$-7.61^{+0.8}_{-0.71}$	
				11814 (2010)	$6.54^{+1.01}_{-1.04}$	
				11815 (2010)	$-7.59^{+0.79}_{-0.84}$	
				11816 (2010)	$-3.98^{+0.8}_{-0.76}$	
				11817 (2010)	$-7.3^{+0.45}_{-0.36}$	
				20191 (2018)	$-7.28^{+1.01}_{-1.12}$	
				20192 (2018)	$-6.62^{+0.78}_{-0.81}$	
				20193 (2019)	$-7.6^{+1.06}_{-1.15}$	
				20194 (2019)	$-13.7^{+0.93}_{-1.01}$	
		MEG	Si XIV	Total (XX)	$-7.01^{+0.17}_{-0.21}$	
				2708 (2002)	$-7.67^{+0.36}_{-0.72}$	
				11814 (2010)	$6.31^{+0.86}_{-0.36}$	
				11815 (2010)	$-7.66^{+0.68}_{-0.71}$	
				11816 (2010)	$-3.27^{+0.47}_{-0.5}$	
				11817 (2010)	$-6.74^{+0.85}_{-0.52}$	
				20191 (2018)	$-6.31^{+0.42}_{-0.9}$	
				20192 (2018)	$-7.89^{+0.81}_{-0.56}$	

Table 4
(Continued)

Source	Exp. Mode	Grating	Ion	Obs Id (Year of Obs)	EW[a] (mA)	Variable
				20193 (2019)	$-6.08^{+0.7}_{-0.75}$	
				20194 (2019)	$-12.56^{+0.72}_{-1.00}$	
	CC	HEG	S XVI	Total (XX)	$-2.8^{+0.5}_{-0.38}$	
				11818 (2010)	$-2.17^{+0.49}_{-0.72}$	
				13197 (2011)	$-3.73^{+0.76}_{-0.69}$	
		MEG	S XVI	Total (XX)	$-2.99^{+0.41}_{-0.41}$	
				11818 (2010)	$-3.56^{+1.63}_{-0.59}$	
				13197 (2011)	$-3.99^{+0.71}_{-0.69}$	
	TE	HEG	S XVI	Total (XX)	$-4.75^{+0.27}_{-0.26}$	
				2708 (2002)	$-5.44^{+0.6}_{-0.79}$	
				11814 (2010)	$-2.25^{+0.7}_{-0.96}$	
				11815 (2010)	$-4.89^{+1.03}_{-1.03}$	
				11816 (2010)	$-2.15^{+0.75}_{-1.19}$	
				11817 (2010)	$-3.05^{+0.53}_{-0.6}$	
				20191 (2018)	$-3.93^{+0.75}_{-0.67}$	
				20192 (2018)	$-7.0^{+0.654}_{-1.0}$	
				20193 (2019)	$-5.25^{+0.49}_{-1.18}$	
				20194 (2019)	$-6.43^{+0.74}_{-0.17}$	
		MEG	S XVI	Total (XX)	$-4.52^{+0.28}_{-0.12}$	
				2708 (2002)	$-4.54^{+0.42}_{-0.71}$	
				11814 (2010)	$-3.42^{+0.97}_{-0.7}$	
				11815 (2010)	$-4.69^{+0.71}_{-0.67}$	
				11816 (2010)	$-2.54^{+0.81}_{-0.18}$	
				11817 (2010)	$-3.89^{+0.89}_{-0.47}$	
				20191 (2018)	$-4.52^{+0.57}_{-0.51}$	
				20192 (2018)	$-4.86^{+0.38}_{-0.9}$	
				20193 (2019)	$-3.89^{+0.54}_{-0.88}$	
				20194 (2019)	$-9.90^{+0.6}_{-0.5}$	
Cygnus X-1	CC	HEG	Ne X	Total (XX)	$-2.52^{+0.2}_{-0.19}$	Yes
				1511 (2000)	$-0.69^{+0.23}_{-2.42}$	
				2415 (2001)	$-2.34^{+0.33}_{-1.2}$	
				3407 (2001)	$-1.0^{+0.4}_{-0.3}$	
				3724 (2002)	$-5.87^{+0.31}_{-0.54}$	
				3815 (2003)	$-1.0^{+0.3}_{-0.4}$	
				12314 (2010)	-1.56	
				12472 (2011)	-12.76	
		MEG	Ne X	Total (XX)	$-1.74^{+0.36}_{-0.22}$	
				1511 (2000)	$-4.32^{+1.69}_{-0.32}$	
				2415 (2001)	$-2.27^{+0.49}_{-0.56}$	
				3407 (2001)	-0.78	
				3724 (2002)	$-4.75^{+0.45}_{-0.72}$	
				3815 (2003)	$-2.39^{+0.17}_{-0.77}$	
				12314 (2010)	-22.23	
				12472 (2011)	-739.59	
	CC	HEG	Si XIV	Total (XX)	$-4.59^{+0.15}_{-0.13}$	
				1511 (2000)	$-5.46^{+0.92}_{-0.2}$	
				2415 (2001)	$-3.78^{+0.12}_{-0.65}$	
				3407 (2001)	$-2.33^{+0.25}_{-0.33}$	
				3724 (2002)	$-11.03^{+0.66}_{-0.04}$	
				3815 (2003)	$-5.35^{+0.2}_{-0.19}$	
				12314 (2010)	$-1.05^{+0.7}_{-0.7}$	
				12472 (2011)	-2.44	
		MEG	Si XIV	Total (XX)	$-6.07^{+0.12}_{-0.12}$	
				1511 (2000)	$-5.96^{+0.49}_{-0.82}$	
				2415 (2001)	$-5.03^{+0.56}_{-0.21}$	
				3407 (2001)	$-3.34^{+0.29}_{-0.24}$	
				3724 (2002)	$12.24^{+0.75}_{-0.014}$	
				3815 (2003)	$-5.68^{+0.36}_{-0.02}$	

Table 4
(Continued)

Source	Exp. Mode	Grating	Ion	Obs Id (Year of Obs)	EW[a] (mA)	Variable
				12314 (2010)	-0.16	
				12472 (2011)	$-1.72^{+0.39}_{-0.76}$	
	TE	HEG	Si XIV	Total (XX)	$-5.47^{+0.19}_{-0.46}$	
				107 (1999)	$-30.64^{+12.02}_{-21.63}$	
				2741 (2002)	$-44.67^{+11.39}_{-20.46}$	
				2742 (2002)	$-46.75^{+11.51}_{-14.55}$	
				2743 (2002)	$-161.89^{+9.5}_{-11.18}$	
				3814 (2003)	$-9.43^{+0.72}_{-0.37}$	
				8525 (2008)	$-10.89^{+0.80}_{-0.41}$	
				9847 (2008)	$-8.62^{+0.60}_{-1.09}$	
				11044 (2010)	-1750.88	
				12313 (2010)	$-95.24^{+54.83}_{-42.55}$	
				13219 (2011)	$-86.07^{+47.48}_{-42.48}$	
				16735 (2016)	$-3.29^{+0.65}_{-0.02}$	
		MEG	Si XIV	Total (XX)	$-4.63^{+0.25}_{-0.25}$	
				107 (1999)	$-416.89^{+12.19}_{-364.02}$	
				2741 (2002)	$-683.04^{+23.01}_{-1316.14}$	
				2742 (2002)	$-4.31^{+2.29}_{-5.04}$	
				2743 (2002)	$-742.67^{+29.5}_{-1659.5}$	
				3814 (2003)	$-10.30^{+1.02}_{-0.29}$	
				8525 (2008)	$-9.48^{+0.38}_{-1.04}$	
				9847 (2008)	$-7.61^{+0.57}_{-1.14}$	
				11044 (2010)	-3.84	
				12313 (2010)	$-733.76^{+17.14}_{-471.24}$	
				13219 (2011)	$-757.86^{+13.30}_{-986.21}$	
				16735 (2016)	$-6.43^{+1.71}_{-1.71}$	
	CC	HEG	S XVI	Total (XX)	$-2.69^{+0.24}_{-0.23}$	
				1511 (2000)	$-3.17^{+1.01}_{-0.54}$	
				2415 (2001)	$-1.00^{+0.31}_{-0.31}$	
				3407 (2001)	$-5.34^{+2.83}_{-2.99}$	
				3724 (2002)	$-7.19^{+1.5}_{-0.03}$	
				3815 (2003)	$-3.54^{+0.39}_{-0.39}$	
				12314 (2010)	-30	
				12472 (2011)	$-1.36^{+0.35}_{-0.97}$	
		MEG	S XVI	Total (XX)	$-2.85^{+0.34}_{-0.21}$	
				1511 (2000)	$-4.66^{+1.12}_{-1.55}$	
				2415 (2001)	$-2.29^{+0.65}_{-0.9}$	
				3407 (2001)	$-0.42^{+0.39}_{-0.39}$	
				3724 (2002)	-6.98	
				3815 (2003)	$-3.57^{+0.44}_{-0.39}$	
				12314 (2010)	-1302	
				12472 (2011)	$-1.09^{+0.59}_{-0.59}$	
	TE	HEG	S XVI	Total (XX)	$-3.19^{+0.34}_{-0.34}$	
				107 (1999)	-0.94	
				2741 (2002)	$-10.53^{+2.53}_{-4.13}$	
				2742 (2002)	$-1.50^{+1.18}_{1.01}$	
				2743 (2002)	$-1.05^{+0.92}_{-0.95}$	
				3814 (2003)	$-4.84^{+0.31}_{-1.01}$	
				8525 (2008)	$-4.11^{+0.53}_{-0.77}$	
				9847 (2008)	$-5.42^{+1.47}_{-1.14}$	
				11044 (2010)	$-0.76^{+0.39}_{-0.53}$	
				12313 (2010)	-1.54	
				13219 (2011)	$-0.80^{+1.58}_{-0.29}$	
				16735 (2016)	$-2.67^{+1.24}_{-1.02}$	
		MEG	S XVI	Total (XX)	$-2.21^{+0.25}_{-0.29}$	
				107 (1999)	$-17.46^{+9.01}_{-15.64}$	
				2741 (2002)	$-2.89^{+1.44}_{-1.11}$	
				2742 (2002)	$-3.06^{+1.03}_{-2.08}$	
				2743 (2002)	$-1.19^{+0.44}_{-1.19}$	

Table 4
(Continued)

Source	Exp. Mode	Grating	Ion	Obs Id (Year of Obs)	EW[a] (mA)	Variable
				3814 (2003)	$-4.23^{+0.47}_{-0.47}$	
				8525 (2008)	$-4.20^{+0.97}_{-0.59}$	
				9847 (2008)	$-3.18^{+0.96}_{-0.37}$	
				11044 (2010)	-6.63	
				12313 (2010)	-8.85	
				13219 (2011)	$-1.06^{+1.95}_{-0.12}$	
				16735 (2016)	$-2.54^{+0.54}_{-0.49}$	

Note.
[a] The 1σ errors are given; otherwise 1σ upper limits are quoted.

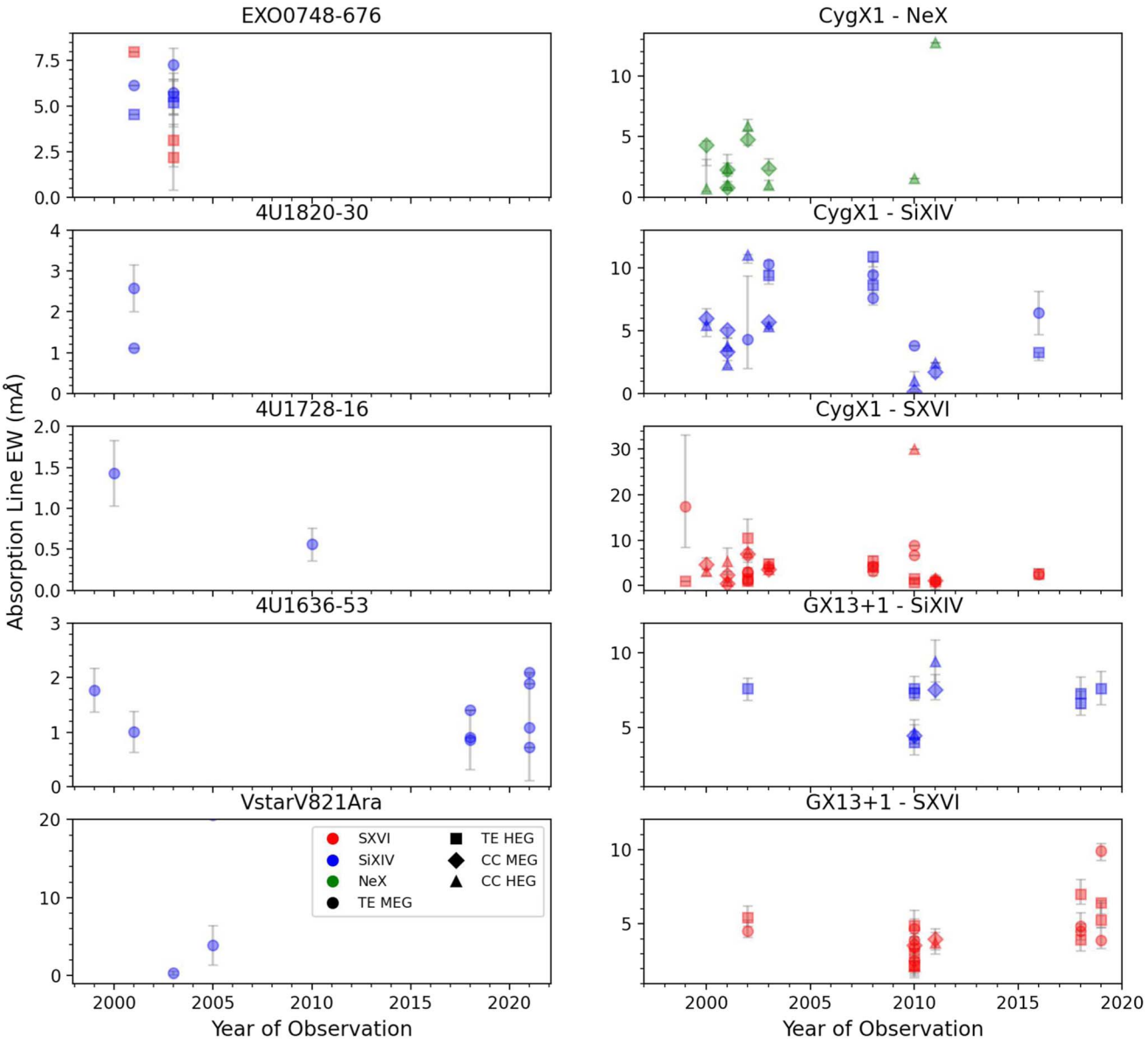

Figure 3. Temporal variation of Ne X, Si XIV, and S XVI lines detected at the 3σ significance level across different XRB sources, showing the 1σ errors and 1σ upper limits. The observed lines exhibit clear variability over time, except for S XVI in the EXO 0748-676 sightline, where the variability remains inconclusive due to a limited number of data points and a short observational time gap. The data points without error bars indicate the 1σ upper limit. Summary: the variability of these detected lines indicates that these lines are most likely originating from variable XRB sources, not from diffuse ISM.

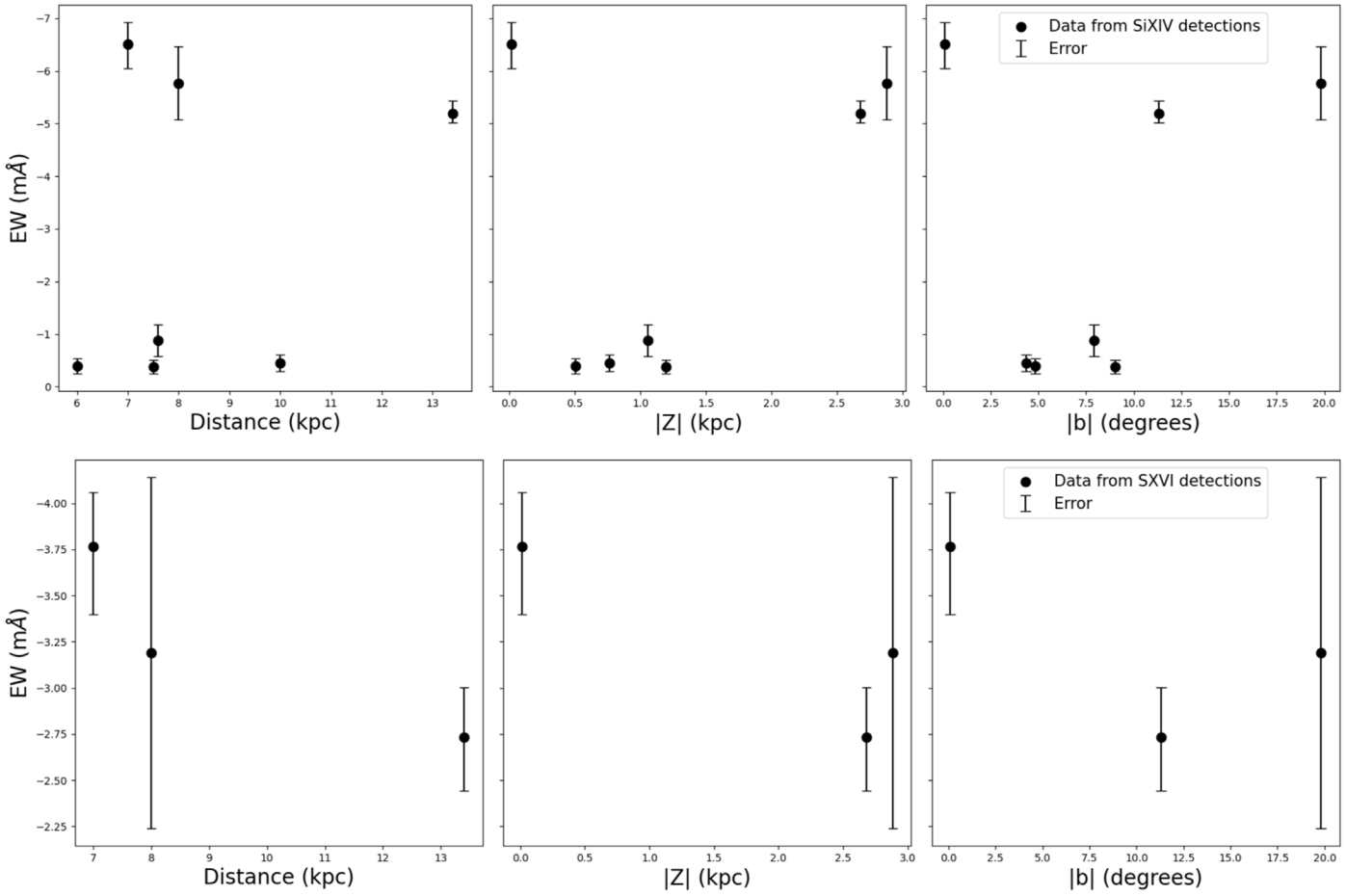

Figure 4. The EW of Si XIV (top) in seven XRB sightlines and S XVI (bottom) lines in three XRB sightlines as a function of distance from us (left), height above the Galactic plane (middle), and Galactic latitude (right). Ne X has been detected only in one XRB sightline, and therefore a correlation study is not possible and is not shown here. Summary: we find no clear correlation between the EW and distance, height, and latitude. The lack of clear correlation suggests that these lines do not originate from the diffuse ISM.

still cannot say whether this gas is in the extraplanar region or in the extended CGM.

6. Conclusion

We aimed to explore the presence of supervirial gas at $\log(T/\mathrm{K}) \sim 7.5$ using high-resolution X-ray spectra from Chandra's HETG observations of 27 XRBs (Table 1). This study was motivated by the need to understand the distribution and origin of this hot gas phase, which remains debated since its unexpected discovery. By searching for signatures of this gas with S XVI Kα, Si XIV Kα, and Ne X Kα absorption lines, we sought to determine if this gas component is present in the diffuse ISM or is in the extraplanar region or in the extended CGM. Our analysis led to the following key findings:

1. *Limited Detection.* Highly ionized absorption lines were detected in only 7 out of the 30 XRB spectra (3 in A. Lara-DI et al. 2024 and 27 in this paper), indicating that the supervirial gas is not abundantly present in the diffuse ISM (Figure 2 and Table 2). Therefore, even if all the detected lines were assigned to the diffuse ISM, the covering fraction of the hot gas would be $<25\%$.
2. *Intrinsic Broad Features.* Two of the detected sources showed broad absorption lines, suggesting that these features are intrinsic to the XRB systems rather than originating from a diffuse ISM (Figure 2 and Table 2). However, we cannot conclude the same for the other 5 XRBs based on line width.
3. *Line Variability.* All the detected lines, except for the S XVI line in the EXO 0748-676 sightline, exhibit temporal variability, reinforcing the hypothesis that these absorption features are tied to the dynamic environments around these variable XRB sources (Figure 3). For EXO 0748-676, noncoinciding data in 2003 suggests variability, but we cannot have a definite conclusion due to a limited number of observations.
4. *Lack of Correlation.* We found no significant correlation between the EW of detected absorption lines and the distance, height, and latitude of the XRBs, again implying that the detected gas is not a part of a homogeneous diffuse ISM (Figure 4).

From previous quasar absorption studies, it was difficult to infer the location of the supervirial gas; it could be anywhere from the ISM to the extraplanar region and/or in the extended

CGM. With the critical test of absorption studies of Galactic XRBs in this paper, we rule out ISM as a possible location of this gas phase. Our work suggests that the supervirial temperature gas must reside in regions beyond the ISM. This may be an extraplanar region above the ISM or the extended outer CGM.

Acknowledgments

M.R acknowledges support from the Center for Cosmology and Particle Physics (CCAPP) fellowship at Ohio State University. M.R. also acknowledges the Aspen Center for Physics and Simons Foundation, as this work was performed in part at the Aspen Center for Physics, which is supported by a grant from the Simons Foundation (1161654, Troyer). S.M. is grateful for the grant provided by the National Aeronautics and Space Administration (NASA) through Chandra Award Number AR0-23014X issued by the Chandra X-ray Center, which is operated by the Smithsonian Astrophysical Observatory for and on behalf of the National Aeronautics Space Administration under contract NAS8-03060. S.M. is also grateful for the NASA ADAP grant 80NSSC22K1121. S.D. acknowledges support from the NASA Hubble Fellowship and KIPAC Fellowship of Kavli Institute for Particle Astrophysics and Cosmology, Stanford University. Y.K. acknowledges support from grant PAPIIT-UNAM IN102023. We gratefully acknowledge support through the NASA ADAP grants 80NSSC24K0626 and 80NSSC22K0480 to AG.

ORCID iDs

Manami Roy https://orcid.org/0000-0001-9567-8807
Smita Mathur https://orcid.org/0000-0002-4822-3559
Sanskriti Das https://orcid.org/0000-0002-9069-7061
Armando Lara-DI https://orcid.org/0000-0001-6995-2366
Yair Krongold https://orcid.org/0000-0001-6291-5239
Anjali Gupta https://orcid.org/0000-0003-1880-1474

References

Bhattacharyya, J., Das, S., Gupta, A., Mathur, S., & Krongold, Y. 2023, ApJ, 952, 41
Bisht, M. S., Nath, B. B., & Mathur, S. 2024, ApJ, 975, 49
Bluem, J., Kaaret, P., Kuntz, K. D., et al. 2022, ApJ, 936, 72
Das, S. 2024, ApJL, 963, L48
Das, S., Mathur, S., Gupta, A., Krongold, Y., et al. 2021, ApJ, 918, 83
Das, S., Mathur, S., Gupta, A., Nicastro, F., & Krongold, Y. 2019a, ApJ, 887, 257
Das, S., Mathur, S., Nicastro, F., & Krongold, Y. 2019b, ApJL, 882, L23
Fang, T., Buote, D., Bullock, J., & Ma, R. 2015, ApJS, 217, 21
Gatuzz, E., García, J. A., & Kallman, T. R. 2021, MNRAS, 504, 4460
Gupta, A., Kingsbury, J., Mathur, S., et al. 2021, ApJ, 909, 164
Gupta, A., Mathur, S., Kingsbury, J., Das, S., & Krongold, Y. 2023, NatAs, 7, 799
Gupta, A., Mathur, S., Krongold, Y., Nicastro, F., & Galeazzi, M. 2012, ApJL, 756, L8
Henley, D. B., Shelton, R. L., Kwak, K., Joung, M. R., & Mac Low, M.-M. 2010, ApJ, 723, 935
Lara-DI, A., Krongold, Y., Mathur, S., et al. 2024, MNRAS, 533, 287
Lara-DI, A., Mathur, S., Krongold, Y., Das, S., & Gupta, A. 2023, ApJ, 946, 55
Mathur, S. 2022, in Handbook of X-ray and Gamma-ray Astrophysics, ed. C. Bambi & A. Santangelo (Singapore: Springer)
McClain, R. L., Mathur, S., Das, S., Krongold, S., & Gupta, A. 2024, MNRAS, 527, 5093
Nicastro, F., Senatore, F., Gupta, A., et al. 2016a, MNRAS, 457, 676
Nicastro, F., Senatore, F., Krongold, Y., Mathur, S., & Elvis, M. 2016b, ApJL, 828, L12
Nicastro, F., Zezas, A., Drake, J., et al. 2002, ApJ, 573, 157
Ponti, G., Zheng, X., Locatelli, N., et al. 2023, A&A, 674, A195
Richter, P., Nuza, S. E., Fox, A. J., et al. 2017, A&A, 607, A48
Rogantini, D., Costantini, E., Mehdipour, M., et al. 2021, A&A, 645, A98
Roy, M., Su, K.-Y., Mathur, S., & Stern, J. 2024, arXiv:2409.17252
Sembach, K., Wakker, B., Savage, B., et al. 2003, ApJS, 146, 165
Tumlinson, J., Peeples, M. S., & Werk, J. K. 2017, ARA&A, 55, 389
Tumlinson, J., Thom, C., Werk, J. K., et al. 2011, Sci, 334, 948
Vijayan, A., & Li, M. 2022, MNRAS, 510, 568
Werk, J. K., Prochaska, J. X., Cantalupo, S., et al. 2016, ApJ, 833, 54
Williams, R. J., Mathur, S., & Nicastro, F. 2005, AAS Meeting, 207, 203.04